

# EXAMINATION OF DEBRIS LOADING EFFECTS ON TORNADO DYNAMICS USING A LARGE-EDDY SIMULATION MODEL AND W-BAND MOBILE RADAR MEASUREMENTS

David Bodine<sup>1,2,3,\*</sup>, Takashi Maruyama<sup>4</sup>, Robert D. Palmer<sup>2,3</sup>, Caleb J. Fulton<sup>3,5</sup>, and Howard B. Bluestein<sup>2</sup>

<sup>1</sup> Advanced Study Program, NCAR, Boulder, CO, U.S.A.

<sup>2</sup> School of Meteorology, University of Oklahoma, Norman, OK, U.S.A.

<sup>3</sup> Advanced Radar Research Center, University of Oklahoma, Norman, OK, U.S.A.

<sup>4</sup> Disaster Prevention Research Institute, Kyoto University, Kyoto, Japan

<sup>5</sup> School of Electrical and Computer Engineering, University of Oklahoma, Norman, OK, U.S.A.

## 1. INTRODUCTION

Visual and radar observations often reveal large amounts of debris surrounding tornadoes. Tornadoes frequently develop clouds of dust, soil, and sand surrounding a condensation funnel, and larger debris are sometimes visible (e.g., wood boards, tree branches). In addition to visual observations of debris, lofted debris produce a prominent polarimetric radar signature called the tornadic debris signature (TDS; Ryzhkov et al. 2002, 2005). Considerable variability exists in TDS characteristics due to changes in tornado damage severity (Ryzhkov et al. 2005; Schultz et al. 2012; Bodine et al. 2013), or geographic differences (Van Den Broeke and Jauernic 2014). Thus, debris amounts, types, and sizes may vary significantly among tornadoes, or even throughout a tornado's lifetime.

Recent studies have suggested that near-surface debris loading affects tornado dynamics. Near-surface debris loading is particularly important because tornado dynamics are sensitive to changes in corner-flow dynamics (Lewellen et al. 2000; Lewellen and Lewellen 2007a,b). Because maximum debris loading occurs in the near-surface layer, momentum exchange between air and debris could result in changes in near-surface wind speeds. To investigate debris loading effects of sand-sized particles, Lewellen et al. (2004), Gong (2006), and Lewellen et al. (2008) simulated the effects of debris loading on tornado dynamics using a Large-Eddy Simulation (LES) model. Lewellen et al. (2008) found that debris loading ( $D_L$ , defined as the ratio of the mass of debris and air) in the corner flow region could exceed 1, leading to significant momentum transfer between air and debris. As a result, their simulations showed that peak tangential velocities are reduced by 20 – 50 percent for high debris loading cases, and suction vortices are weakened or eliminated.

While these simulations suggest that debris loading may affect tornado dynamics, observational studies of debris loading have yet to be conducted. To conduct observational studies of debris loading, methods are required to estimate particle concentrations in tornadoes, and such methods have not been developed. Doppler radar measurements

have been extensively used to examine temporal and spatial changes in tornado wind speeds and provide a potential avenue for simultaneously measuring debris loading and spatial and temporal changes in tornado wind speeds. However, because debris centrifuging effects introduce errors in Doppler velocity measurements (Dowell et al. 2005; Lewellen et al. 2008; Bodine et al. 2014), using Doppler radars to evaluate the response of tornado wind speeds to debris loading is complicated by evolution of the three-dimensional debris distribution (e.g., size, type). Thus, radar-based analyses of debris loading must account for debris centrifuging effects on Doppler velocity, or debris distributions must remain approximately constant with time.

In the present study, debris loading effects of sand-sized particles are examined using a LES model (Maruyama 2011). Sensitivity tests are performed to simulate a large range of particle fluxes expected in nature and assess changes in tornado wind speeds. Using output from the LES model, radar variables are simulated using T-matrix calculations to ascertain relationships between debris loading and radar variables such as equivalent reflectivity factor and attenuation. Finally, methods are developed to estimate maximum bounds on debris loading based on attenuation estimates obtained from tornado observations from the University of Massachusetts W-band mobile radar.

## 2. LES MODEL AND RADAR SIMULATION

In this section, the configuration of the LES model is described, including the drag force feedback model for debris. Then, methods to simulate attenuation using T-matrix calculations and LES model output are presented.

The LES model is based on RIAM-COMPACT developed at Kyushu University (Uchida and Ohya 2003). Maruyama (2011) discuss the application of this LES model for tornado simulations and debris trajectory calculations. In this study, the LES model uses 155, 155, and 89 grid points in the x-, y-, and z-dimensions, respectively. A fine grid is used within the core flow of the tornado to provide maximum resolution, and a staggered grid is used outside the core flow. The LES model is non-dimensional, so results can be dimensionalized by choosing a characteristic velocity,  $V_0$

\* Corresponding author address: David Bodine, NCAR, 3450 Mitchell Lane, Boulder, CO 80302; e-mail: dbodine@ucar.edu

(150 m s<sup>-1</sup> in this study). The boundary conditions of the LES model simulate a tornado vortex chamber, and exhibit geometric ratios similar to past chamber experiments and within the range of expected values in nature (Church et al. 1979).

The debris trajectory calculation and drag force feedback models are described in detail in Bodine (2014) but will be summarized here. The drag force model is based on Newton's third law, assuming that if a drag force is exerted on a particle, a equal reaction force must occur in the opposite direction. The body force exerted by one debris element is given by:

$$f_{xi} = \frac{1}{2} \rho C_D A (u_i - u_{di}) |u_i - u_{di}|, \quad (1)$$

where  $C_D$  is the drag force coefficient,  $A$  is the area of the debris,  $\rho$  is the air density, and  $u_i$  and  $u_{di}$  are the air and debris velocities, respectively. The body force per unit mass,  $F_{xi}$ , can then be expressed as:

$$F_{xi} = \frac{1}{\rho V_{grid}} \sum_{n=1}^N f_{xi,n}, \quad (2)$$

where  $V_{grid}$  is the grid cell volume, and  $N$  is the number of debris elements. The  $F_{xi}$  term can then be subtracted from the spatially filtered Navier-Stokes equation. For small particles (e.g., sand), the maximum number of trajectories that can be computed are on the order of 1 million. Thus, to simulate high concentrations of particles, it is necessary to employ a scaling factor,  $S$ , which is multiplied by  $F_{xi}$  when subtracted from the Navier-Stokes equation. In other words, a single trajectory is allowed to represent  $S$  particles in the simulation.

The trajectory-based drag force model approach to modeling debris loading effects has some advantages and disadvantages. An advantage of this approach is that debris velocity can vary within a grid cell, allowing for some explicit turbulent representation of debris velocity. Moreover, a more realistic size or type distribution of debris can be simulated because  $SF_{xi}$  for multiple debris types or sizes can be summed. On the other hand, the scaling factor approach requires that enough trajectories are computed to accurately represent mean characteristics of debris in a grid cell (e.g., relative velocity). In the simulations herein, most grid cells in the corner flow region contain hundreds or thousands of trajectories, providing robust statistics.

The lack of measurements of dust or sand surface fluxes in tornadoes poses a challenge for debris loading studies. Dust and soil particle fluxes have been measured in wind tunnels and laboratory vortices. Neakrase and Greeley (2010) found that soil particle fluxes varied from 10<sup>-5</sup> – 1 kg m<sup>-2</sup> in laboratory vortices. Given the large range of surface debris fluxes, the sensitivity of vortex dynamics to surface debris fluxes are examined in this study by varying surface debris

fluxes over several orders of magnitude. In the present study, two examples highlighting a low and high debris loading case are presented. For the surface debris parameterization, surface debris fluxes are allowed to vary as near-surface wind speeds change. Debris fluxes are specified as a linear function of the lowest grid cell turbulent kinetic energy, similar to the parameterization by Lewellen et al. (2008).

Equivalent reflectivity factor and attenuation are computed for sand/soil particles using Transmission (T) matrix calculations (Waterman 1969). To compute radar variables using T-matrix calculations, complex relative permittivities of sand particles are specified using measurements from Matzler (1998) for the 3 – 10 GHz range and Gatesman et al. (2005) for frequencies above 10 GHz. The real parts of the complex relative permittivities for dry sand at X band in Matzler (1998) and Gatesman et al. (2005) are within 0.2, showing good agreements between the measurements and minimizing differences between the two experiments (e.g., differences in soil types). Finally, the sand particles are assumed to be spherical. In nature, sand particles can exhibit roughness and some eccentricity, however, the focus here is on mean  $Z_e$  rather than polarimetric radar variables. Thus, it is assumed that the mean  $Z_e$  for a randomly oriented sand particle with slight eccentricity is equal to the  $Z_e$  for an equivalent volume sphere (see Bodine et al. (2014) for a test of this assumption).

Specific attenuation ( $A_H$ , dB km<sup>-1</sup>) is calculated using forward scattering amplitudes ( $f_{hh}$ ) as follows (Oguchi 1973):

$$A_H = 8.686 \lambda \int_{D_{min}}^{D_{max}} \Im(f_{hh}(D)) N(D) dD, \quad (3)$$

where  $D_{min}$  and  $D_{max}$  are the minimum and maximum diameter sizes and  $\lambda$  is the radar wavelength. Equivalent reflectivity factor ( $Z_e$ ) is obtained using backscatter amplitudes ( $s_{hh}$ ) as follows:

$$Z_e = \frac{4\lambda^4}{\pi^4 |K_w|^2} \int_{D_{min}}^{D_{max}} |s_{hh}(D)|^2 N(D) dD, \quad (4)$$

Using the LES model output (e.g., sand particle concentrations), attenuation is computed using an angular weighting function (Doviak and Zrnić 1993).

Geological and agricultural studies have obtained particle size distributions (PSDs) for soils (Tyler and Wheatcraft 1989, 1992). In this study, soil PSDs are specified for initial debris fluxes to provide a more realistic soil PSD in the simulations. Soil particles follow fractal behavior (Turcotte 1986), which allows soil particle distributions to be expressed in the following form:

$$N_s r_s^p = const., \quad (5)$$

where  $N_s$  is the number of soil particles greater than radius,  $r_s$ . For sandy and clay loam soils (Tyler and Wheatcraft 1992),  $p$  has values of 2.646 and 2.832, respectively.

Table 1: Attenuation rates ( $\text{dB km}^{-1}$ ) and equivalent reflectivity factor (dBZ) for dry clay and sandy soils at S, C, X, Ka and W bands for  $D_L$  of 1. Soil particle sizes range from 0.1 – 1 mm radii.

Frequency Band	Clay ( $\text{dB km}^{-1}$ )	Sand ( $\text{dB km}^{-1}$ )	Clay (dBZ)	Sand (dBZ)
S	2.0	2.0	47.6	48.3
C	2.0	2.0	47.6	48.3
X	1.8	1.8	47.5	48.3
Ka	16.8	19.1	47.3	48.0
W	400.2	465.8	43.5	43.9

Table 2: Attenuation rates ( $\text{dB km}^{-1}$ ) for wet clay and sandy soils at S, C, X, Ka and W bands for  $D_L$  of 1 (fractional water content of 20%). Soil particle sizes range from 0.1 – 1 mm radii.

Frequency Band	Clay ( $\text{dB km}^{-1}$ )	Sand ( $\text{dB km}^{-1}$ )	Clay (dBZ)	Sand (dBZ)
S	3.4	3.4	51.9	52.7
C	7.8	7.8	51.9	52.7
X	20.5	20.5	51.7	52.6
Ka	297.1	307.0	51.2	52.2
W	1859.5	2004.5	44.4	46.1

Using the sandy and clay loam soil PSDs, equivalent radar reflectivity factor and attenuation are computed over a range of common weather radar frequencies for the range of sand-sized particles examined in this study (0.1 – 1 mm radii). Equivalent reflectivity factor and attenuation for  $1.2 \text{ kg m}^{-3}$  (equivalent to  $D_L = 1$ ) of dry and wet sandy and clay loam soils are shown in Tables 1 and 2, with the wet soil case using a fractional volume ( $f_v$ ) of 20%. Because sand particles satisfy the Rayleigh condition at S, C, and X bands, equivalent radar reflectivity factors and attenuation rates are similar except for small differences caused by frequency dependence of complex relative permittivities for sand (Matzler 1998). At Ka and W bands, however, Mie scattering effects increase attenuation due to scattering, causing much higher attenuation rates. At W band, attenuation rates for dry and wet soils are hundreds of  $\text{dB km}^{-1}$  for  $D_L$  of 1. Moreover, equivalent radar reflectivity factor is also lower at higher frequencies because large particles exhibit Mie scattering whereas at lower frequencies the same particles are Rayleigh scatterers and Z increases as a function of  $D^6$ .

### 3. DEBRIS LOADING SIMULATIONS

In this section, simulations of debris loading using realistic PSDs are presented for a low and high debris loading case. Simulated radar variables are then obtained from model particle concentrations.

Two simulations are shown to encompass a possible range of debris loading cases where debris loading effects are small (D1) and large (D2). For each simulation, 1 million trajectories are computed for each of the following sand particle radii: 0.1, 0.25, 0.5, 0.75, and 1 mm. The scaling factors are determined by the particle size distribution for a sandy loam soil. A summary of simulation statistics are presented in Table 3. The D2 initial scaling factors are 20 times greater than D1. However, the negative feedback associated with reduced TKE in response to debris loading reduces surface debris fluxes (i.e., a mean  $D_L$  only three times greater than D1). Lewellen et al. (2008) found a similar negative feedback mechanism associated with reduced near-surface wind speeds and lower sand particle fluxes.

For the low debris loading case (Simulation D1), sand particle loadings on the order of  $100 \text{ g m}^{-3}$  occur within the volume enclosed by  $r < 50 \text{ m}$  and  $z < 50 \text{ m}$  (Figure 1, left column). Maximum debris loading occurs within this region for all particle sizes. At higher altitudes, small sand particles exhibit greater contributions to debris loading within the vortex core whereas larger sand particles are centrifuged outward and are subsequently recycled into the inflow. Simulated equivalent reflectivity factor at W band is shown in the right column of Figure 1. Maximum  $Z_e$  occurs in the lowest grid with a value of 36.7 dBZ, and  $Z_e$  remains as high

Table 3: Summary of statistics from debris loading cases where debris loading effects are small and large. Maximum and mean  $D_L$ , maximum  $\Delta U$ , and minimum  $\Delta V$  and  $\Delta W$  are shown.

Case	Max. $D_L$	Mean $D_L$	Max $\Delta U$ ( $\text{m s}^{-1}$ )	Min $\Delta V$ ( $\text{m s}^{-1}$ )	Min $\Delta W$ ( $\text{m s}^{-1}$ )
D1	0.20	0.005	3.9	-4.8	-4.3
D2	1.42	0.018	18.1	-16.7	-8.4

as 29.3 dBZ at 100 m AGL. Sand particles in this simulation fall within the Mie scattering region because the maximum Rayleigh diameter is 0.19 mm, thus resulting in complex relationships between  $Z_e$  and particle size. Nonetheless, sand particles with radii greater than or equal to 0.5 mm exhibit the greatest contributions to  $Z_e$ .

Because the maximum amount of debris loading occurs in the corner flow region, the maximum momentum transfer through drag forces and resulting velocity change occurs here. Radial, tangential and vertical velocities, and pressure variables for Simulation D1 are shown in the left column of Figure 2, and differences between these quantities and the control simulations are shown in the right column. Within the region of maximum debris loading, the maximum tangential velocity reduction is  $4.8 \text{ m s}^{-1}$ , and a concomitant small decrease in pressure occurs ( $\Delta P = -0.8 \text{ hPa}$ ). Lofted debris also reduces the inward radial momentum of the corner flow within a very shallow layer, causing a maximum reduction of inflow velocities of  $3.9 \text{ m s}^{-1}$ . However, corner flow radial velocities exhibit very small changes elsewhere. Vertical velocities are reduced in the region of higher debris loading associated with larger particles. The larger terminal fall speeds of the 0.5-mm and 1-mm sand particles likely contribute to greater drag and reaction forces within this region. However, vertical velocity changes are also small (less than  $5 \text{ m s}^{-1}$ ). A region of positive vertical velocity change occurs along the central axis of the vortex, likely in response to a vertical perturbation pressure gradient force induced by the tangential velocity reduction.

For the high debris loading case (Simulation D2), sand particle loading exceeds  $1 \text{ kg m}^{-3}$  within a shallow layer in the corner flow region, and particle loadings exceeding  $100 \text{ g m}^{-3}$  reach 150 m AGL (Figure 3). Similar to the low debris loading case, all sand particles contribute significantly to corner flow debris loading, although the near-surface debris loading exhibits a maximum value for the 0.5-mm radius particles. A maximum W-band equivalent reflectivity factor of 47.5 dBZ occurs near the surface, and the maximum value at 100 m AGL is 33.1 dBZ.

Higher debris loading in Simulation D2 leads to greater momentum exchange through drag forces and larger velocity changes. The maximum reduction in tangential velocities of  $16.7 \text{ m s}^{-1}$  occurs within the area of maximum debris loading, and smaller reductions in tangential velocity of a few  $\text{m s}^{-1}$  extend to 300 m AGL (Figure 4). Because concentrations of sand particles aloft are small, the reduction in tangential velocities aloft likely occurs in response to changes in the corner flow region. Momentum exchange between air and sand particles reduce the parcel's angular momentum as it passes through the corner flow region, which may result in lower tangential velocities aloft as the air parcel turns upward into the core flow. The magnitude of corner flow radial velocities are reduced out to  $r=200 \text{ m}$  where debris concentrations are low ( $\sim 10 \text{ g m}^{-3}$ ), and drag-induced accelerations are small. Reduced inflow velocities here may result from the increase in central core pressure of 3.8 hPa and subsequent decrease in the radial pressure gradient force.

Using debris concentrations from Simulations D1 and D2, simulated two-way attenuation through the vortex center is computed at multiple radar elevation angles and ranges (Figure 5). For Simulation D1, two-way attenuation of 10 – 15 dB (30 – 40 dB) occurs for low elevation angle scans for dry (wet) sand at close ranges. Thus, some attenuation should be observed at W band for cases where debris loading effects are small (on the order of a few  $\text{m s}^{-1}$ ). For the large debris loading case, much greater attenuation occurs, exceeding 100 dB for both dry and wet sand. Such large values of attenuation would cause signal extinction through the tornado vortex for any practical radar system.

Based on these simulations, the observing requirements for measuring debris loading are low elevation angles (e.g.,  $< 0.4^\circ$ ) and close ranges. For the high debris loading case, however, substantial attenuation would still occur at higher elevation angles and/or at greater ranges. Nevertheless, because the maximum debris loading occurs in the corner flow region, optimal scanning strategies should attempt to observe this region. Of course, near-surface radar measurements are complicated by several factors, such as beam blockage or ground clutter contamination.

#### 4. W-BAND RADAR OBSERVATIONS

In this section, a cursory exploration of radar-based methods to estimate sand or soil particle concentrations is presented. Sand or soil particle concentrations are estimated for dust devils and tornadoes using W-band radar reflectivity factor and estimated attenuation rates.

Several field experiments have measured in-situ concentrations of lofted particles in dust devils. Using lidar observations, Renno et al. (2004) measured particle concentrations of  $100 \text{ mg m}^{-3}$ . Metzger et al. (2011)

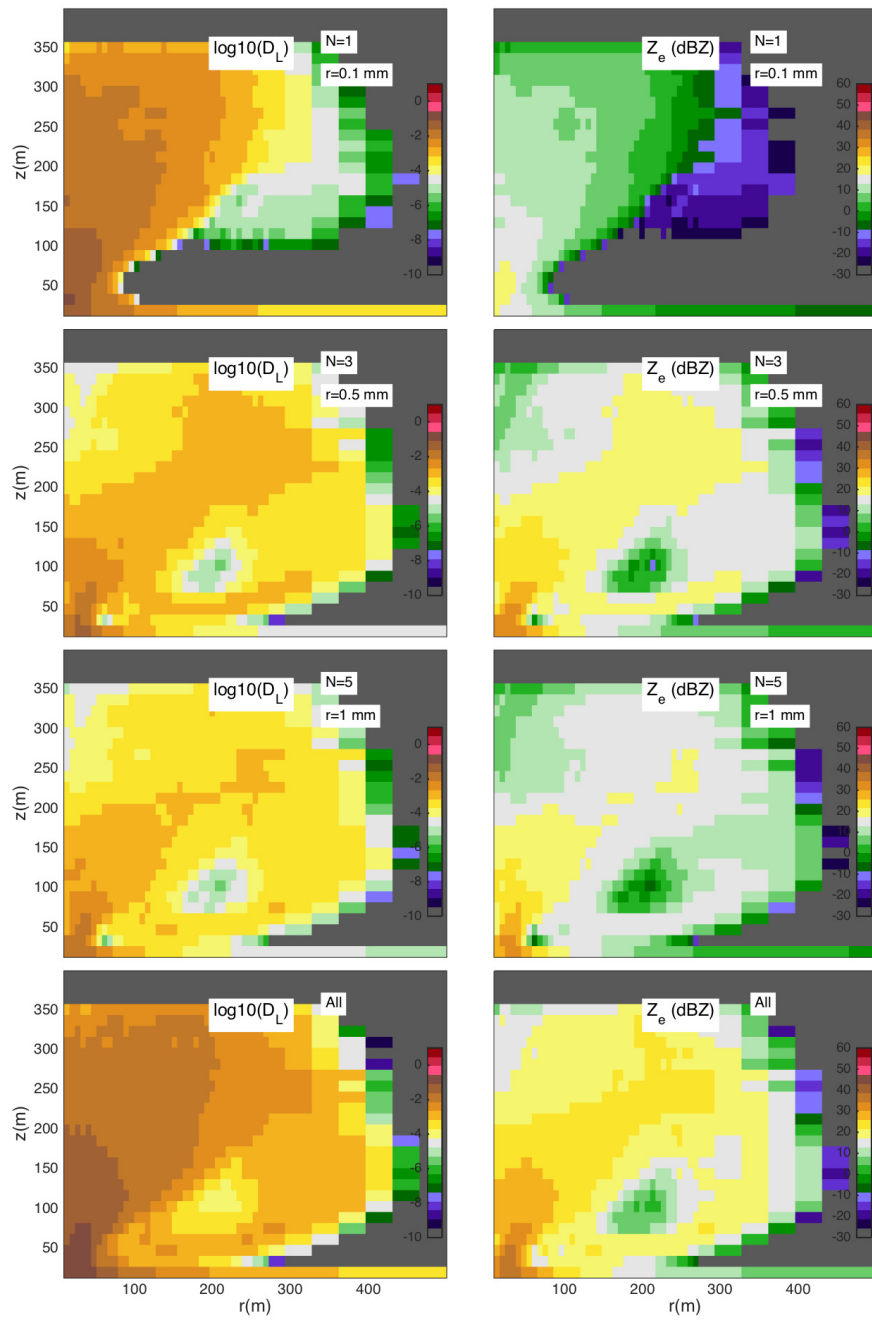


Figure 1:  $\log_{10}$  of debris loading (left column) and W-band equivalent reflectivity factor (dBZ) for 0.1-mm, 0.5-mm, and 1-mm radius sand particles, and debris loading and equivalent reflectivity factor for all particles in Simulation D1. Maximum debris loading occurs within the volume enclosed by  $r < 50$  m and  $z < 50$  m.

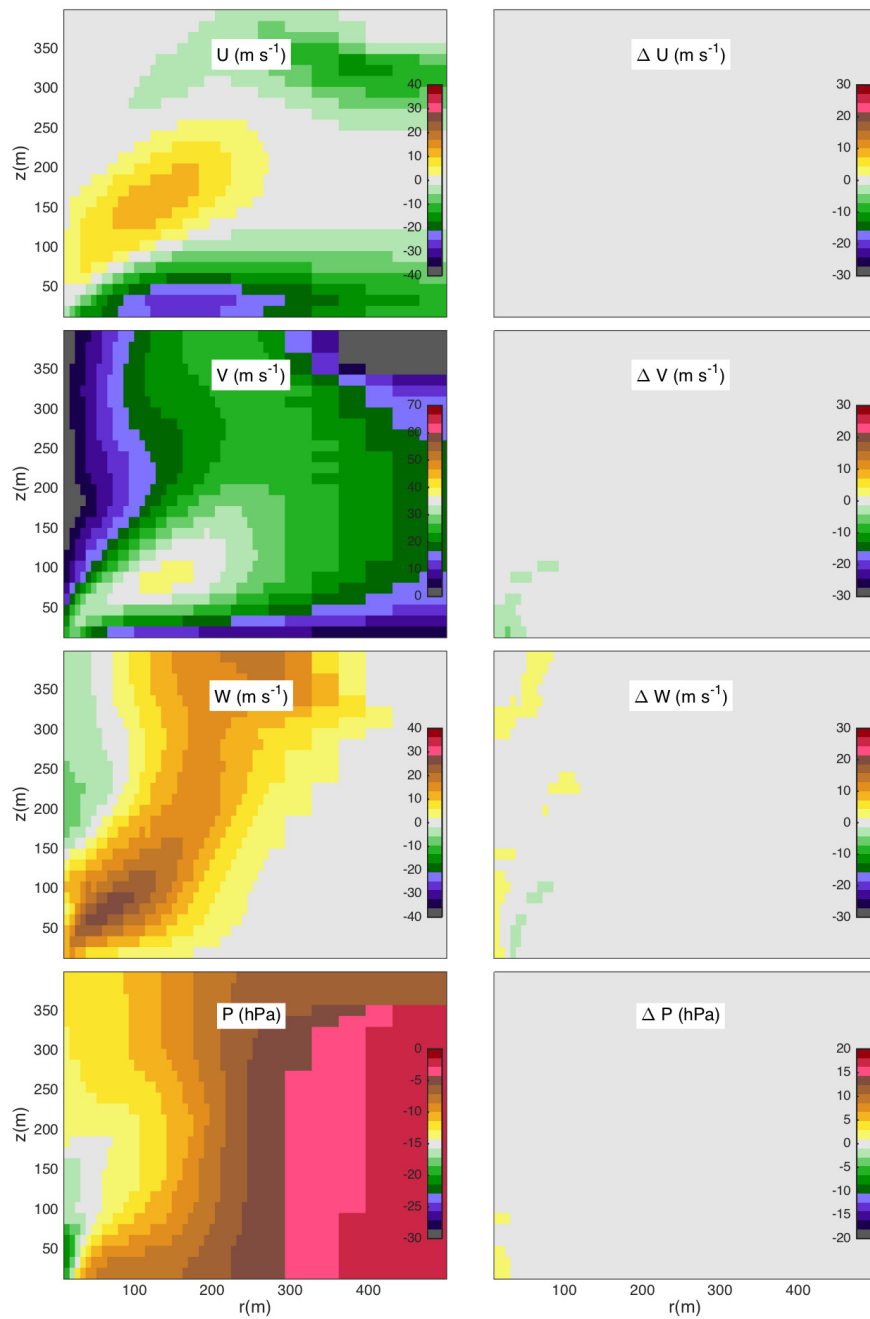


Figure 2: The left column shows mean Simulation D1 radial, tangential and vertical velocity ( $\text{m s}^{-1}$ ), and pressure (hPa), and the right column shows the difference between these mean quantities for Simulation D1 and the control (no debris loading) experiment. The largest velocity and pressure changes are observed in the corner flow region where the maximum debris loading occurs.

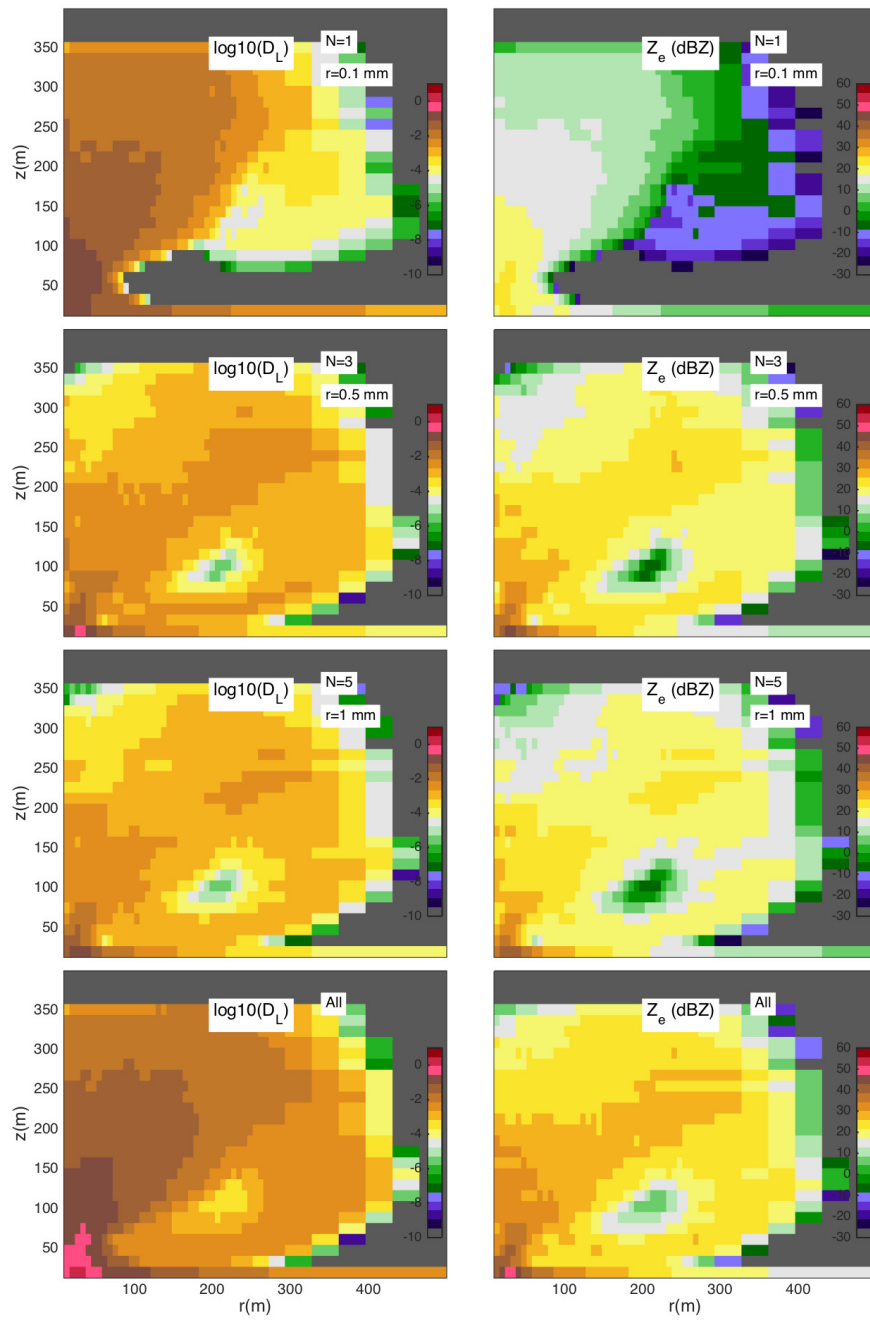


Figure 3:  $\log_{10}$  of debris loading (left column) and W-band equivalent reflectivity factor (dBZ) for 0.1-mm, 0.5-mm, and 1-mm radius sand particles, and debris loading and equivalent reflectivity factor for all particles in Simulation D2. Peak debris loading exceeds 1 in Simulation D2.

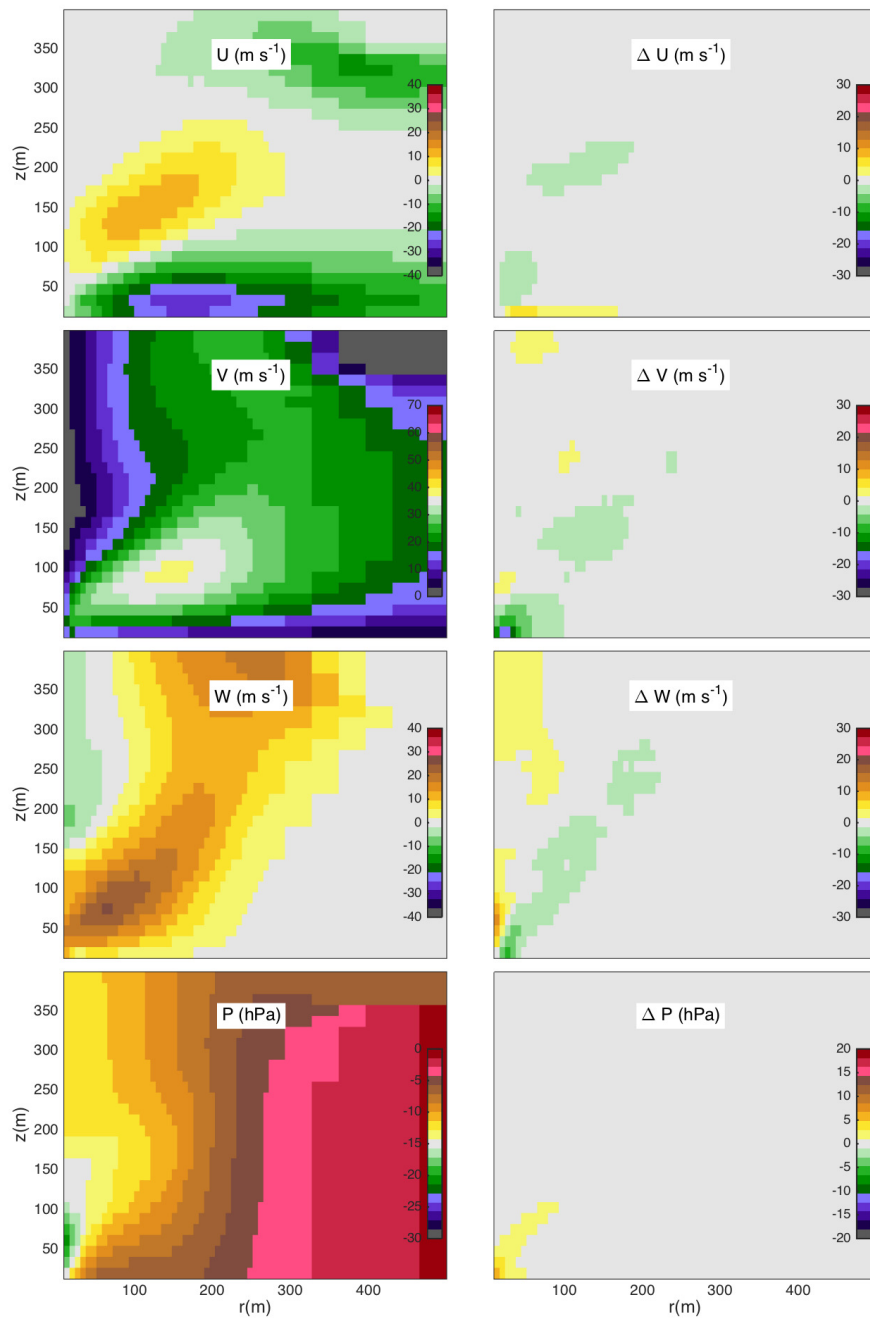


Figure 4: The left column shows mean Simulation D2 radial, tangential and vertical velocity ( $\text{m s}^{-1}$ ), and pressure (hPa), and the right column shows the difference between these mean quantities for Simulation D2 and the control experiment. Compared to Simulation D1, larger magnitude velocity changes occur in response to higher debris loading. Inflow and tangential velocity reductions exceed  $10 \text{ m s}^{-1}$  in the corner flow, and reduced tangential and vertical velocities extend into the core flow aloft.

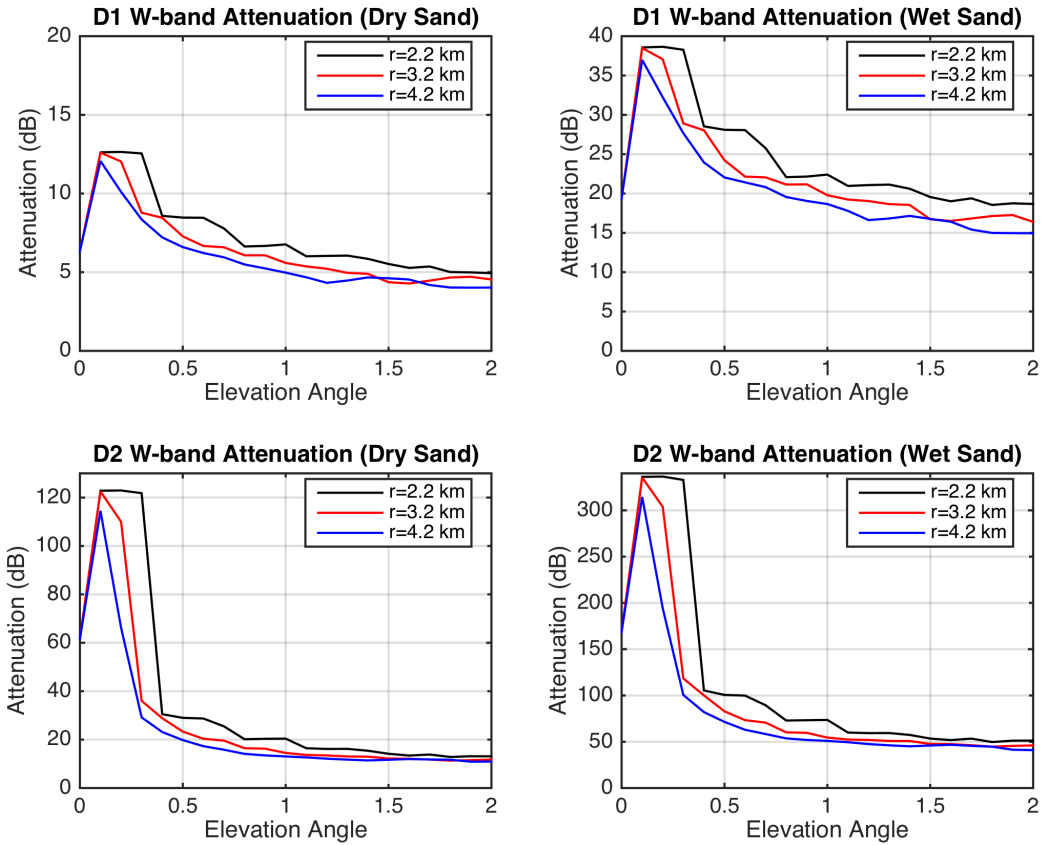


Figure 5: Simulated two-way attenuation (dB) through the center of the vortex for Simulations D1 (top panels) and D2 (bottom panels). Attenuation is shown as a function of range (distance from the radar to the vortex center) and elevation angle, and is presented for dry (left) and wet (right) sand particles. For Simulation D1, 10 – 15 dB (30 – 40 dB) of two-way attenuation occurs for dry (wet) sand. For Simulation D2, two-way attenuation exceeds 100 dB at low elevation angles for both dry and wet sand.

measured in-situ particle concentrations in 33 dust devils in Nevada and Arizona, and measured mean particle concentrations between  $8 - 875 \text{ mg m}^{-3}$  with a mean value of  $296 \text{ mg m}^{-3}$ . Based on the T-matrix-based value of equivalent reflectivity factor for sand (Table 1) at W-band, the range of particle concentrations from Metzger et al. (2011) corresponds to  $Z_e$  between -7.9 and 12.5 dBZ.

Bluestein et al. (2004) collected W-band radar observations of four dust devils in Texas. Examining W-band reflectivity factor data (e.g., their Figures 4 – 7), maximum  $Z_e$  appears to be in the range of -15 – 0 dBZ. These  $Z_e$  values correspond to particle concentrations of  $1.5 - 48 \text{ mg m}^{-3}$ . Because in-situ particle concentrations were not measured, radar-estimated particle concentrations cannot be compared to measured concentrations. Nevertheless, radar-estimated particle loads encompass a portion of the range measured by Metzger et al. (2011), even though their measurements were obtained in Nevada and Arizona. Lower estimated particle concentrations compared to Metzger et al. (2011) could be explained by attenuation, uncertainty in particle size distributions, geographic differences, or differences in dust devil intensity. Metzger et al. (2011) made measurements in a warmer and drier climate, possibly leading to higher sand particle concentrations by increasing soil erodibility or producing more intense dust devils (e.g., due to greater insolation). Future experiments could collect in-situ particle concentrations with collocated radars and/or lidars to better understand the relationship between  $Z_e$  and sand/soil particle concentrations.

For cases where significant changes in tornado dynamics are observed (e.g., Simulation D2), strong W-band attenuation is expected. To estimate particle concentrations, attenuation rates are computed across the tornado vortex by assuming radial symmetry of radar reflectivity factor. Under this assumption, the attenuation rate,  $A$ , is calculated as follows:

$$A = \frac{Z_{HH}(i - \Delta n) - Z_{HH}(i + \Delta n)}{2n\Delta r}, \quad (6)$$

where  $i$  is the range gate index,  $\Delta n$  is the half-interval over which attenuation is computed, and  $\Delta r$  is the range gate spacing. For example, if a symmetric vortex produces a unattenuated radar reflectivity factor of 20 dBZ at a 500-m radius, and measured (attenuated) radar reflectivity factor at a 500-m radius from the vortex center farthest from the radar is 10 dBZ, the computed attenuation rate is  $10 \text{ dB km}^{-1}$ . In addition to the symmetry assumption, particle concentration estimates are based on the assumption that sand particles cause the observed attenuation. Other scatterers may contribute (perhaps significantly) to observed attenuation rates, and thus attenuation-based estimates of particle concentrations are an *upper-bound* on sand particle concentrations.

On 5 June 1999, Bluestein et al. (2003) collected W-band radar observations of a tornado near Bassett, Nebraska. A photograph of the tornado at 2017 CDT shows a prominent debris cloud (cf. Figure 2a; Bluestein et al. 2003). Using photogrammetry, they estimated a debris cloud width of 150 m. The width of the weak-echo hole varies considerably for different scan times, and is actually wider than the estimated width of the debris cloud at 2016:52 UTC. Thus, scatterers within the debris cloud are associated with a minimum in  $Z_{HH}$ . Surrounding the tornado, areas of precipitation are prominent and appear to be responsible for some attenuation.

The attenuation estimation technique is applied to the 2016:52 UTC  $1^\circ$  elevation scan. The vortex center is located 2.3 km from the radar with an estimated beam height of 40 m AGL. As an estimator of symmetry, a root-mean squared (RMS) error of azimuthal  $Z_{HH}$  differences are computed (if  $Z_{HH}$  is a function of  $r$ , the theoretical RMS error for azimuthal  $\Delta Z_{HH}$  would be 0). The RMS error for the 2016:52 UTC scan is 5.3 dB. Computed  $\Delta Z_{HH}$  values along radials close to the vortex center at 2016:52 UTC do not exhibit a clear positive or negative trend, and  $\Delta Z_{HH}$  magnitudes are within the errors estimated for the symmetry assumption. Thus, the ambiguous radial  $\Delta Z_{HH}$  and inferred lack of attenuation suggests that debris loading is small, and significant attenuation indicative of high debris loading is not observed (i.e., Simulation D2).

The next attenuation W-band case is from the 3 May 1999 Verden, Oklahoma case (Bluestein and Pazmany 2000). The tornado exhibited a well-developed debris cloud, and produced significant structural damage around 1856 – 1900 CDT (Bluestein and Pazmany 2000, cf., Fig. 3,5). They estimated a debris cloud width of 650 m, and W-band Doppler velocities exceeded  $70 \text{ m s}^{-1}$ . The RMS error estimate based on the azimuthal  $\Delta Z_{HH}$  is 3.4 dB for the 1900:13 CDT  $1^\circ$  elevation scan. Attenuation effects across the ring-shaped reflectivity signature associated with the tornado are evident. Significant attenuation may be occurring to the north of the tornado as  $Z_{HH}$  decreases rapidly beyond 4 km range, however this attenuation occurs beyond the visible debris cloud. Using the reflectivity difference across a 500-m distance, attenuation is estimated to be 6 dB over 500 m, or  $12 \text{ dB km}^{-1}$ , or a  $D_L$  of  $0.03 \pm 0.017$ . It should be emphasized that all particles in the tornado contribute to attenuation, and thus the contribution of the sand particles to attenuation constitutes some (unknown) fraction of the observed attenuation. In particular, the tornado produced significant damage close to the radar scan time, and thus large debris effects on attenuation cannot be ruled out.

## 5. CONCLUSIONS

Using numerical simulations and W-band radar observations, debris loading effects on tornado dynamics are examined. Debris loading effects are simulated using a Large-Eddy Simulation model with a trajectory-based drag force feedback model and a realistic particle size distribution for soils. In agreement with previous findings, significant changes in near-surface wind speeds are observed when near-surface debris loading exceeds 1. Using LES model output, equivalent reflectivity factor and attenuation are computed. For the high debris loading simulation, significant attenuation exceeding 100 dB occurs at W-band and would lead to signal extinction. In contrast, the low debris simulation exhibits much smaller, but still noticeable attenuation on the order of tens of dB. T-matrix calculations also demonstrate that sand particle wetting or soil moisture could significantly change attenuation rates.

W-band radar observations from dust devils and tornadoes are examined to estimate debris loading. For dust devils, W-band radar reflectivity factor is used to estimate sand particle concentrations based on T-matrix calculations, and sand particle concentrations of  $1.5 - 48 \text{ mg m}^{-3}$  are obtained. These particle concentrations are within the range of measured particle concentrations in dust devils in Arizona, although toward the lower end. Attenuation, differences in particle size distributions, or physical reasons for higher particle concentrations in Arizona (e.g., more intense dust devils or higher surface fluxes due to greater soil aridity) may account for these differences.

Attenuation rates are estimated from W-band radar data for two tornado cases at close ranges and low elevation angles. For the Bassett, Nebraska tornado, attenuation rates did not exceed estimated errors due to asymmetries in reflectivity, and thus debris loading is likely small. Greater attenuation rates are observed in the Verden, Oklahoma tornado, and correspond to an estimated debris loading of 0.03. Such values are comparable to debris loading observed in simulation D1. It should be emphasized that the estimated debris loading assumes that the observed attenuation is caused by sand or soil particles, and thus is likely an overestimate of the actual sand or soil particle concentration. In the small sample size of cases considered herein, debris loading in tornadoes with prominent debris clouds is small, and would tend to have small effects on tornado dynamics.

Direct measurements of attenuation in tornadoes, perhaps at multiple frequencies simultaneously, would be useful and more robust than symmetry-based estimates of attenuation. Such measurements might be possible with bistatic radars measuring line-of-sight, path-integrated attenuation. Experiments with multiple frequencies and dual-polarization radars may be useful for resolving the

contribution to attenuation of rain drops given the greater differences in complex relative permittivity for rain compared to sand. Measurements of phase delay caused by refractive index variations along a line-of-sight propagation path could also be fruitful and would minimize issues associated with beam blockage (i.e., decreasing radar reflectivity factor with range resulting from beam blockage). Future experiments should also collect soil samples to obtain information about particle size distributions, electromagnetic characteristics, and wetness to refine the T-matrix calculations for specific cases.

Future simulations will expand the modeling capabilities of the LES model to include different debris types with a drag force feedback model. Initial tests have been conducted with a 6-degree of freedom (DOF) trajectory model (Richards et al. 2008; Maruyama and Noda 2012) which uses orientation-dependent drag and moment force coefficients from wind tunnel measurements, thus enabling more realistic trajectories of non-spherical particles. Future LES experiments will also examine the sensitivity of the upper boundary condition (i.e., low-level mesocyclone scale updraft) to buoyancy effects caused by debris loading. Given the simplified upper boundary conditions used in the LES model, however, high-resolution numerical simulations of both the parent thunderstorm and tornado vortex (e.g., Xue et al. 2007; Schenkman et al. 2014) may have greater potential for investigating the impact of debris loading and associated negative buoyancy on the tornado vortex and storm-scale updraft.

## 6. ACKNOWLEDGMENTS

This study is based upon work supported by the National Science Foundation under Grants No. AGS-1303685 and OISE-1209444. The first author is supported by the National Center for Atmospheric Research (NCAR) Advanced Study Program. NCAR is sponsored by the National Science Foundation. The authors thank Tammy Weckwerth for comments on a draft of this paper.

## References

- Bluestein, H. B., W.-C. Lee, M. Bell, C. C. Weiss, and A. L. Pazmany, 2003: Mobile Doppler radar observations of a tornado in a supercell near Bassett, Nebraska, on 5 June 1999. Part II: Tornado-vortex structure. *Mon. Wea. Rev.*, **131**, 2968–2984.
- Bluestein, H. B. and A. L. Pazmany, 2000: Observations of tornadoes and other convective phenomena with a mobile, 3-mm wavelength, Doppler radar: The Spring 1999 Field Experiment. *Bull. Amer. Meteor. Soc.*, **81**, 2939–2951.

- Bluestein, H. B., C. C. Weiss, and A. L. Pazmany, 2004: Doppler radar observations of dust devils in Texas. *Mon. Wea. Rev.*, **132**, 209–224.
- Bodine, D., 2014: *Polarimetric radar observations and numerical simulations of tornadic debris*. Ph.D. thesis, University of Oklahoma.
- Bodine, D., M. R. Kumjian, R. D. Palmer, P. L. Heinselman, and A. V. Ryzhkov, 2013: Tornado damage estimation using polarimetric radar. *Wea. Forecasting*, **28**, 139–158.
- Bodine, D. J., R. D. Palmer, T. Maruyama, C. J. Fulton, and B. L. Cheong, 2014: Dual-frequency simulations of radar observations of tornadoes. *27th Conf. on Severe Local Storms*, Amer. Meteor. Soc.
- Church, C. R., J. T. Snow, G. L. Baker, and E. M. Agee, 1979: Characteristics of tornado-like vortices as a function of swirl ratio: A laboratory investigation. *J. Atmos. Sci.*, **36**, 1755–1776.
- Doviak, R. J. and D. S. Zrnić, 1993: *Doppler Radar and Weather Observations*. Dover Publications, Mineola, New York, 2nd edition.
- Dowell, D. C., C. R. Alexander, J. M. Wurman, and L. J. Wicker, 2005: Centrifuging of hydrometeors and debris in tornadoes: Radar-reflectivity patterns and wind-measurement errors. *Mon. Wea. Rev.*, **133**, 1501–1524.
- Gatesman, A. J., T. M. Goyette, J. C. Dickinson, R. H. Giles, J. Waldman, J. Sizemore, R. M. Chase, and W. E. Nixon, 2005: Polarimetric backscattering behavior of ground clutter at X, Ka, and W band. *Proc. SPIE 5808*, 428–439.
- Gong, B., 2006: *Large-eddy simulation of the effects of debris on tornado dynamics*. Ph.D. thesis, West Virginia Univ.
- Lewellen, D. C., B. Gong, and W. S. Lewellen, 2004: Effects of debris on near-surface tornado dynamics. *22nd Conf. on Severe Local Storms*, Amer. Meteor. Soc., ed.
- 2008: Effects of finescale debris on near-surface tornado dynamics. *J. Atmos. Sci.*, **65**, 3247–3262.
- Lewellen, D. C. and W. S. Lewellen, 2007a: Near-surface intensification of tornado vortices. *J. Atmos. Sci.*, **64**, 2176–2194.
- 2007b: Near-surface vortex intensification through corner flow collapse. *J. Atmos. Sci.*, **64**, 2195–2209.
- Lewellen, D. C., W. S. Lewellen, and J. Xia, 2000: The influence of a local swirl ratio on tornado intensification near the surface. *J. Atmos. Sci.*, **57**, 527–544.
- Maruyama, T., 2011: Simulation of flying debris using a numerically generated tornado-like vortex. *J. Wind Eng. Ind. Aerodynamics*, **99**, 249–256.
- Maruyama, T. and M. Noda, 2012: Tornado-borne debris. *J. Appl. Wind Engr.*, **37**, 124–129.
- Matzler, C., 1998: Microwave permittivity of dry sand. *IEEE Tran. Geosci. Remote Sensi.*, **36**, 317–319.
- Metzger, S. M., M. R. Balme, M. C. Towner, B. J. Bos, T. J. Ringrose, and M. R. Patel, 2011: In situ measurements of particle load and transport in dust devils. *Icarus*, **214**, 766–772.
- Neakrase, L. D. V. and R. Greeley, 2010: Dust devils in the laboratory: Effect of surface roughness on vortex dynamics. *J. Geophys. Res.*, **115**.
- Oguchi, T., 1973: Attenuation and phase rotation of radio waves due to rain: Calculations at 19.3 and 34.8 GHz. *Radio Sci.*, **8**, 31 – 38.
- Renno, N. O., V. J. Abreu, J. Koch, P. H. Smith, O. K. Hartogensis, H. A. R. DeBruin, D. Burose, G. T. Delory, W. M. Farrell, C. J. Watts, J. Garatuza, M. Parker, and A. Carswell, 2004: MATADOR 2002: A pilot field experiment on convective plumes and dust devils. *J. Geophys. Res.*, **109**, E07001.
- Richards, P. J., N. Williams, B. Laing, M. McCarty, and M. Pond, 2008: Numerical calculation of the three-dimensional motion of wind-borne debris. *J. Wind Eng. Ind. Aerodynamics*, **96**, 2188–2202.
- Ryzhkov, A., D. Burgess, D. Zrnić, T. Smith, and S. Giangrande, 2002: Polarimetric analysis of a 3 May 1999 tornado. *Preprints, 21th Conf. on Severe Local Storms*, Amer. Meteor. Soc., ed., San Antonio, TX.
- Ryzhkov, A. V., T. J. Schuur, D. W. Burgess, and D. S. Zrnić, 2005: Polarimetric tornado detection. *J. Appl. Meteor.*, **44**, 557–570.
- Schenkman, A. D., M. Xue, and M. Hu, 2014: Tornadogenesis in a high-resolution simulation of the 8 May 2003 Oklahoma City supercell. *J. Atmos. Sci.*, **71**, 130–154.
- Schultz, C. J., S. E. Nelson, L. D. Carey, L. Belanger, B. C. Carcione, C. B. Darden, T. Johnstone, A. L. Molthan, G. J. Jedlovec, E. V. Schultz, C. C. Crowe, and K. R. Knupp, 2012: Dual-polarization tornadic debris signatures Part II: Comparisons and caveats. *Electronic J. Operational Meteor.*, **13**, 138–158.
- Turcotte, D. L., 1986: Fractals and fragmentation. *J. Geophys. Res.*, **91**, 1921–1926.
- Tyler, S. W. and S. W. Wheatcraft, 1989: Application of fractal mathematics to soil water retention estimation. *Soil. Sci. Soc. of America*, **53**, 987–995.
- 1992: Fractal scaling of soil particle-size distributions: Analysis and limitations. *Soil. Sci. Soc. of America*, **56**, 362–369.

Uchida, T. and Y. Ohya, 2003: Large-eddy simulation of turbulent airflow over complex terrain. *J. Wind Eng. Ind. Aerodynamics*, **91**, 219 – 229.

Van Den Broeke, M. S. and S. T. Jauernic, 2014: Spatial and temporal characteristics of polarimetric tornadic debris signatures. *J. Appl. Meteor. Climatol.*, **53**, 2217–2231.

Waterman, P. C., 1969: Scattering by dielectric obstacles. *Alta Frequenza, (Speciale)*, 348–352.

Xue, M., S. Liu, and T. Yu, 2007: Variational analysis of oversampled dual-Doppler radial velocity data and application to the analysis of tornado circulations. *J. Atmos. Oceanic Technol.*, **24**, 403–414.